THE JOURNAL OF PHYSICAL CHEMISTRY Letters

Letter

Cite This: J. Phys. Chem. Lett. 2018, 9, 2049−2055

pubs.acs.org/JPCL

Hydrogen Evolution Reaction at Anion Vacancy of Two-Dimensional Transition-Metal Dichalcogenides: Ab Initio Computational Screening

Joohee Lee,[†,§] Sungwoo Kang,[†,§] Kanghoon Yim,[†,∥] Kye Yeop Kim,[†,⊥] Ho Won Jang,[†] Youngho Kang,[*,‡] and Seungwu Han[*,†]

[†]Department of Materials Science and Engineering and Research Institute of Advanced Materials, Seoul National University, Seoul 08826, Korea

[‡]Materials Modeling and Characterization Department, Korea Institute of Materials Science, Changwon 51508, Korea

Supporting Information

ABSTRACT: The catalytic activity for the hydrogen evolution reaction (HER) at the anion vacancy of 40 2D transition-metal dichalcogenides (TMDs) is investigated using the hydrogen adsorption free energy (ΔG_H) as the activity descriptor. While vacancy-free basal planes are mostly inactive, anion vacancy makes the hydrogen bonding stronger than clean basal planes, promoting the HER performance of many TMDs. We find that $ZrSe_2$ and $ZrTe_2$ have similar ΔG_H as Pt, the best HER catalyst, at low vacancy density. ΔG_H depends significantly on the vacancy density, which could be exploited as a tuning parameter. At proper vacancy densities, MoS_2, $MoSe_2$, $MoTe_2$, $ReSe_2$, $ReTe_2$, WSe_2, $IrTe_2$, and $HfTe_2$ are expected to show the optimal HER activity. The detailed analysis of electronic structure and the multiple linear regression results identifies the vacancy formation energy and band-edge positions as key parameters correlating with ΔG_H at anion vacancy of TMDs.

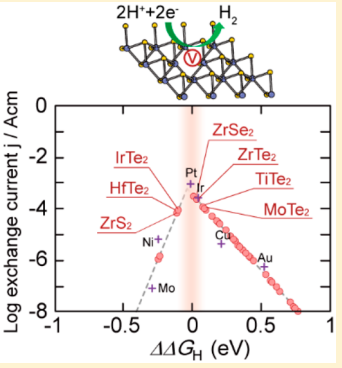

Currently, producing hydrogen, an eco-friendly energy fuel, predominantly relies on the technology using fossil fuels, but it has critical drawbacks such as limited availability of fossil fuels and emission of CO_2 and pollutants during the hydrogen production.[1] Accordingly, significant efforts are put on developing an alternative way to produce hydrogen, which is sustainable as well as environmentally benign.[2] Splitting water, the most abundant resource on earth, may resolve the aforementioned problem of using fossil fuels for hydrogen production. Water molecules decompose into hydrogen and oxygen gas within electrochemical cells operating on the electrical bias or solar energy. Because of strong O−H bonds in water molecules, water splitting requires catalysts that speed up the hydrogen and oxygen evolution reactions (HER and OER, respectively). For decades, Pt has been known to be the best catalyst for HER in water splitting, but the high material cost makes it unsuitable for large-scale applications. As a result, discovering an alternative material of Pt has been the biggest challenge toward the use of hydrogen as a future energy fuel.[3−5]

There are growing interests in 2D transition-metal dichalcogenides (TMDs), particularly MoS_2, as a nonprecious catalyst for HER owing to various advantages such as earth abundance, low cost, high catalytic activity, and stability in the acidic media.[6−21] Because the basal planes of stable TMDs are inert, studies have focused on exploiting active edge sites[20,22,23] or metastable phases.[24−26]

Recently, Li et al. have successfully activated the MoS_2 basal plane by creating sulfur vacancies.[27] It was found that the sulfur vacancies in MoS_2 could increase the catalytic activity for HER by enhancing the hydrogen adsorption, and the activity increased even further when an adequate strain was applied on the defective MoS_2. This motivated much research to introduce vacancies, dopants, and other forms of defects in TMDs for using the material as HER catalysts.[28−30]

While preceding works demonstrated the catalytic activity of MoS_2 with anion vacancies, a question remains whether other TMDs may also exhibit the enhanced HER activity, possibly higher than MoS_2, when defects are introduced. Therefore, it would be timely to carry out an extensive study on anion vacancies in various TMDs and evaluate them in terms of HER activity. In this article, we theoretically explore the HER efficiencies of basal planes and anion vacancy sites of various TMD materials by calculating the hydrogen binding energy, a well-established descriptor for HER.[31−34] We suggest candidate TMDs that are promising for HER when anion vacancies are introduced. Through the detailed analysis of electronic structures, we also identify strong correlation of physical parameters such as the vacancy formation energy and band-edge positions with the adsorption energy of hydrogen to the anion vacancy.

Density functional theory (DFT) calculations are conducted using the Vienna Ab initio Simulation Package (VASP).[35] We

Received: March 7, 2018
Accepted: April 5, 2018
Published: April 5, 2018

DOI: 10.1021/acs.jpclett.8b00712
J. Phys. Chem. Lett. 2018, 9, 2049−2055

use the projector-augmented wave (PAW) method[36] to represent electron−ion interactions, and generalized gradient approximation is chosen for the exchange-correlation functional.[37] The energy cutoff for the plane-wave basis set is chosen to be 450 eV, and the *k*-points for the Brillouin-zone integration are sampled on a mesh grid of 18 × 18 × 1 and 4 × 4 × 1 for unit cells and 4 × 4 supercells, respectively. The ionic positions are relaxed until the magnitude of the force on each atom is reduced to within 0.03 eV/Å. The spin-polarized calculations are performed throughout this work. For TMDs with finite local magnetic moments at the transition-metal ions (VS_2, VSe_2, VTe_2, and $CrTe_2$), we consider ferromagnetic spin configuration. To avoid interactions between repeated images along the *z* axis within the periodic boundary condition, we introduce a vacuum with 20 Å thickness. The spurious dipole interaction between the slabs is corrected by introducing external dipoles.[38]

To select 2D TMDs, we first search Inorganic Crystal Structure Database (ICSD)[39] for compounds with the composition MX_2 (M = metal ion in group 4−12 and 14, X = S, Se, and Te). Excluding 3D materials (usually Pyrite structures) and 2D structures with four-fold coordinated metals such as PdX_2 or GeX_2 (X = S or Se), we identify 40 compositions, as shown in Figure 1a. For possible polymorphs

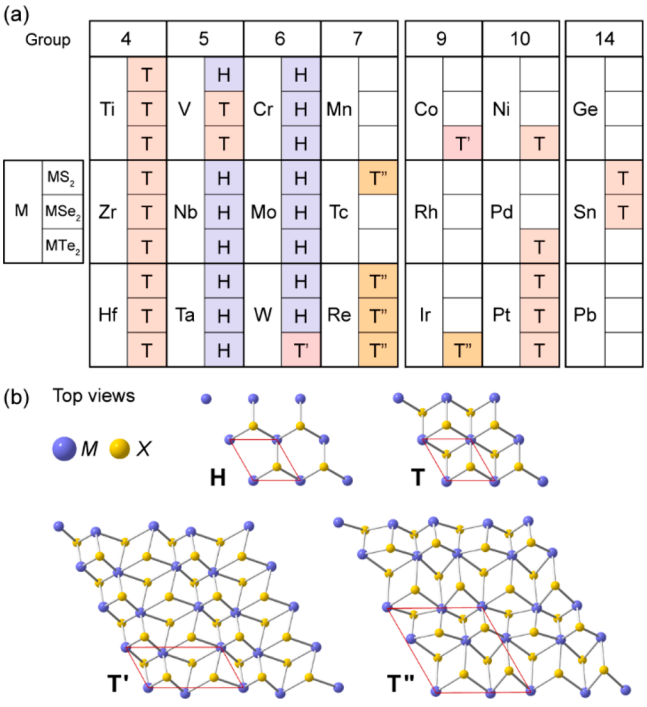

Figure 1. (a) Most stable phases of selected TMD compositions. (b) Top views of polymorphs calculated for each TMD. The H phase (MoS_2 type) has the trigonal prismatic coordination of chalcogen atoms, while the T phase (CdI_2 type) has the octahedral coordination. T′ (WTe_2 type) and T″ ($ReSe_2$ type) phases are distorted T phases.

of each TMD, we consider H, T, T′, and T″ phases, where H and T indicate the trigonal prismatic and octahedral structures, respectively, and T′ and T″ are distorted T phases (see Figure 1b). In the present study, only the most stable phases are studied. We note that some elements may have drawbacks in actual utilization. For instance, Tc is radioactive and Re has extraordinarily low natural abundance.

The hydrogen-adsorption property of both basal plane and *X*-vacancy (V_X) is calculated using supercells containing 16 MX_2 units (i.e., 4 × 4 supercells for H and T phases). V_X is created by removing a chalcogen atom within the supercell, which corresponds to the nominal vacancy density (ρ_V) of 6.25% in the upper chalcogen plane. Further increase in the supercell size barely changed the properties of V_X, meaning that V_X can be regarded as an isolated defect in this concentration. The vacancy formation energy (E_f^V) is calculated as follows

$$E_f^V = E(\text{clean}) - E(V_X) + \mu_X \quad (1)$$

where E(clean) is the total energy of a clean TMD supercell and $E(V_X)$ is the total energy of a supercell including one V_X. In eq 1, μ_X is the chemical potential of X, and it is chosen by employing standard corrosion resistance of X, namely, the condition that the evolution of H_2X gas is equilibrated with 10^{-6} bar at room temperature (see Section 1 in the Supporting Information for details). In the low-symmetry T′ and T″ phases, there exist several inequivalent vacancy sites, and we choose the most stable site with the lowest E_f^V.

Hydrogen adsorption energy (ΔE_H) is computed using the following equation

$$\Delta E_H = E(*H) - E(*) - \frac{1}{2}E(H_2) \quad (2)$$

where E(*H) and E(*) are the total energies of a supercell with and without hydrogen adsorbed on the active site *, respectively, and $E(H_2)$ is the total energy of the hydrogen molecule. For the basal plane, we test every inequivalent *M*-top and *X*-top sites, finding that hydrogen favors the *X*-top site over the *M*-top site for most TMDs, except for nine TMDs ($CoTe_2$, $HfTe_2$, $IrTe_2$, $NbTe_2$, $ReTe_2$, $TaTe_2$, $TiTe_2$, $NiTe_2$, and $ZrTe_2$).

The hydrogen adsorption free energy (ΔG_H) is defined as follows

$$\Delta G_H = \Delta E_H + \Delta E_{ZPE} - T\Delta S \quad (3)$$

where ΔE_{ZPE} is the difference of the zero-point energy and T is the temperature (300 K in the present study). From the normal-mode analysis, we obtain ΔE_{ZPE} of −0.021 eV for MoS_2 when hydrogen is adsorbed on the sulfur vacancy. For simplicity, we use this value in every system because ΔE_{ZPE} changes only slightly over different TMDs.[40,41] In eq 3, ΔS is the entropy change due to the hydrogen adsorption. We assume that the entropy difference between hydrogen-adsorbed TMD and TMD is negligible. This means that $\Delta S \approx -(1/2)\,S^0(H_2)$, where $S^0(H_2)$ is the entropy of H_2 gas at the standard condition (1.36 meV/K from the thermochemical table).[42]

To examine how ΔG_H changes at the large vacancy concentration, we introduce four anion vacancies uniformly in the upper chalcogen layer of the 4 × 4 supercell, which corresponds to 25% of ρ_V. Such a high vacancy concentration could be achieved in experiments by argon plasma treatment.[27] Because the hydrogen coverage (Θ_H) at vacancy sites affects ΔG_H, we first evaluate the equilibrium Θ_H using the Frumkin adsorption isotherm.[43] By assuming a linear relationship between ΔG_H and Θ_H, we find that the equilibrium Θ_H is bigger than 0.8 in the majority of TMDs. As such, we compute ΔE_H at the maximum coverage we can simulate in the given supercell

$$\Delta E_H(\rho_V = 25\%) = E(*4H) - E(*3H) - \frac{1}{2}E(H_2) \quad (4)$$

DOI: 10.1021/acs.jpclett.8b00712
J. Phys. Chem. Lett. 2018, 9, 2049−2055

Table 1 compiles the main computational results. The most stable phase and band gap in our calculations are consistent with previous computation results.[44,45] The group-dependent preference of a specific phase is observed, which is closely related to electronic configuration of the d manifold of transition metals.[46]

Table 1. Main Calculation Results[a]

TMD	phase	E_g (eV)	E_f^V (eV)	$\Delta\Delta G_H$ (6.25%)	$\Delta\Delta G_H$ (25%)	$\Delta\Delta G_H$ (basal)
TiS_2	T	metal	0.68	0.61	0.48	0.54
$TiSe_2$	T	metal	1.54	0.42	0.51	1.00
$TiTe_2$	T	metal	2.36	0.08	0.38	1.10
ZrS_2	T	1.18	2.25	−0.11	−0.38	1.08
$ZrSe_2$	T	0.48	2.37	0.01	−0.31	1.29
$ZrTe_2$	T	metal	2.48	0.03	−0.29	1.20
HfS_2	T	1.28	2.82	−0.42	−0.38	1.30
$HfSe_2$	T	0.58	2.89	−0.25	−0.20	1.50
$HfTe_2$	T	metal	2.85	−0.11	0.07	1.23
VS_2	H	metal	0.96	0.57	1.16	0.85
VSe_2	T	metal	1.19	0.34	0.51	0.74
VTe_2	T	metal	1.85	0.10	0.32	0.61
NbS_2	H	metal	1.12	0.37	0.43	0.15
$NbSe_2$	H	metal	1.64	0.28	0.23	0.59
$NbTe_2$	H	metal	1.93	0.19	0.37	0.61
TaS_2	H	metal	1.46	0.24	0.39	0.33
$TaSe_2$	H	metal	1.73	0.31	0.33	0.69
$TaTe_2$	H	metal	1.43	0.71	0.48	0.58
CrS_2	H	0.93	1.65	0.28	0.21	1.54
$CrSe_2$	H	0.74	2.25	0.18	0.47	1.67
$CrTe_2$	H	0.53	0.51	0.64	1.44	1.15
MoS_2	H	1.81	2.21	0.28	0.03	2.32
$MoSe_2$	H	1.63	2.64	0.20	−0.06	2.52
$MoTe_2$	H	1.27	3.10	0.09	−0.12	2.33
WS_2	H	0.66	2.37	0.41	0.14	2.62
WSe_2	H	0.58	2.70	0.35	0.03	2.69
WTe_2	T′	metal	2.64	−0.24	−0.30	1.15
TcS_2	T″	1.35	1.08	0.74	1.00	1.16
ReS_2	T″	1.43	1.60	0.61	0.41	1.65
$ReSe_2$	T″	1.26	2.24	0.58	−0.09	1.89
$ReTe_2$	T″	0.93	2.92	0.14	0.03	1.59
$CoTe_2$	T′	metal	1.34	0.44	0.75	0.38
$IrTe_2$	T″	0.63	2.72	−0.10	0.31	1.41
$NiTe_2$	T	metal	1.16	0.78	0.82	0.95
$PdTe_2$	T	0.34	1.53	0.77	0.69	1.30
PtS_2	T	1.85	1.28	0.53	0.50	1.36
$PtSe_2$	T	1.42	1.89	0.39	0.37	1.67
$PtTe_2$	T	0.81	2.33	0.30	0.22	1.45
SnS_2	T	1.57	1.35	0.44	0.40	1.17
$SnSe_2$	T	0.87	1.16	0.75	0.50	0.97

[a]Stable phase, band gap (E_g), vacancy formation energy (E_f^V), and hydrogen adsorption free energy relative to that on Pt ($\Delta\Delta G_H$) of anion vacancy at 6.25 and 25% vacancy concentrations and clean basal plane.

Figure 2 shows hydrogen adsorption free energies for clean basal planes and anion vacancies, along with the volcano plot for elemental metals, which was obtained from the relation between experimental exchange currents and theoretical ΔG_H values for Mo, Ni, Pt, Ir, Cu, and Au.[31] For facile comparison, we discuss the catalytic activity based on $\Delta\Delta G_H$ that is ΔG_H relative to that of Pt obtained using the same computational setup

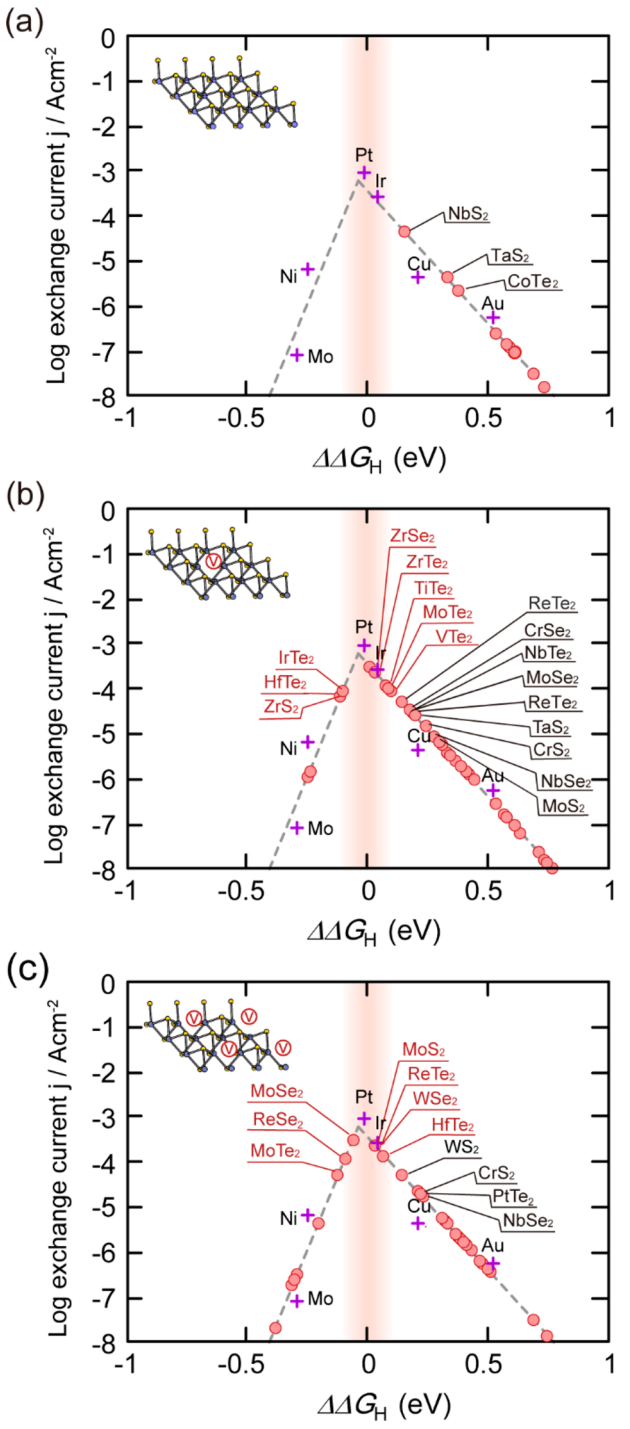

Figure 2. Hydrogen adsorption free energies ($\Delta\Delta G_H$) of (a) clean TMD basal planes and anion vacancies at (b) 6.25 and (c) 25% vacancy concentrations. The volcano plot (dashed lines) for metal catalysts showing the relation between the experimental exchange current and theoretical $\Delta\Delta G_H$ is adopted from previous work.[31] Insets represent atomic structures of clean or defective basal planes used to calculate $\Delta\Delta G_H$ (Ⓥ is the vacancy site). Considering the tunability of $\Delta\Delta G_H$ within a few hundred millielectronvolts by applying strain,[11,27] the sweet spot ($|\Delta\Delta G_H| < 0.1$ eV) is shaded in red to indicate potential candidates more clearly.

$$\Delta\Delta G_H = \Delta G_H - \Delta G_H(\mathrm{Pt}) \quad (5)$$

Because Pt is the best catalyst known to date, we assume that $\Delta\Delta G_H$ close to 0 is the condition for ideal HER catalysts. We

DOI: 10.1021/acs.jpclett.8b00712
J. Phys. Chem. Lett. 2018, 9, 2049−2055

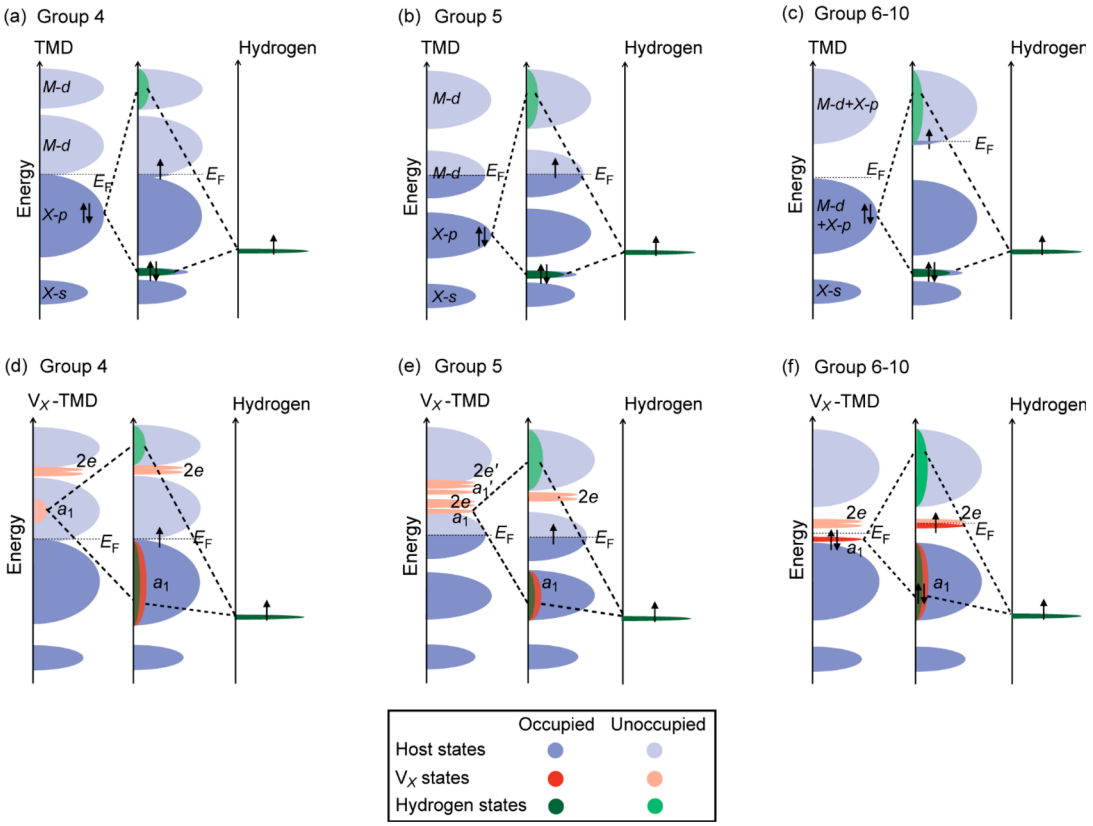

Figure 3. Schematic band diagrams illustrating the interaction between hydrogen with the clean basal planes ((a–c) for group 4, 5, and 6–10 TMDs, respectively) and defective planes ((d–f) for group 4, 5, and 6–10 TMDs, respectively).

note that ΔG_H varies by a few tenths of electronvolts among different exchange-correlation functionals, but the relative differences are well maintained (see Section 2 in the Supporting Information). Therefore, discussions based on $\Delta\Delta G_H$ would not be affected by the choice of exchange-correlation functionals.

$\Delta\Delta G_H$ values on the TMD basal planes are plotted in Figure 2a for the energy range between −1 and 1 eV. Only a few TMDs appear in this range, and the majority of TMD basal planes show significantly large and positive $\Delta\Delta G_H$, consistent with the previous work.[32] This implies that most of the TMD basal planes are HER-inactive due to the unfavorable hydrogen adsorption. Interestingly, all TMDs shown in Figure 2a are metals. This is because it costs less energy to add an extra electron to metallic TMDs than semiconducting TMDs; when hydrogen is adsorbed to the basal plane of TMD, the interaction of the hydrogen state with host states gives rise to the bonding and antibonding states. In metallic systems, an extra electron after filling the bonding state occupies the host state near the Fermi level, as illustrated in Figure 3a,b for group 4 and 5 TMD metals, respectively. On the contrary, in semiconducting TMDs, the lowest empty state to be filled by the excess electron is higher in energy by the band gap (see Figure 3c). This results in the larger energy cost to form a bond with hydrogen in semiconducting TMDs.

Next, we discuss the hydrogen adsorption on TMDs with anion vacancies. When V_X is created, the dangling bonds of neighboring cations hybridize into defect states. The detailed analysis of these states will be useful for understanding the behavior of ΔG_H in various TMDs. Except for group 5 TMDs, three localized defect states are generated: singlet a_1 and doubly degenerate e levels. The energetic position of these levels can be classified depending on the group number of transition metals, as schematically depicted in Figure 3d–f. In group 4 TMDs (Figure 3d), all V_X states appear inside the host states because the large ionicity results in distinct orbital characters of the bands; that is, M-d states mainly constitute the unoccupied bands, while X-p states comprise the occupied bands.[47] In group 6–10 TMDs with the strong covalent bond (Figure 3f), the a_1 defect state is fully occupied. In group 5 TMDs (Figure 3e), three other localized states, also denoted as a_1' and e' states by the group theory, appear above E_F. This originates from significant distortion of the atomic structure around V_X, which leads to localization of cation states in the vicinity of V_X (see Section 3 in Supporting Information).

As shown in Table 1, the adsorption strength of hydrogen on V_X is very different from that on the clean basal plane. The anion vacancy tends to lower $\Delta\Delta G_H$ compared with the basal plane, and, consequently, more TMDs are found in Figure 2b at the low vacancy concentration (ρ_V = 6.25%). Specifically, ZrS_2, $HfTe_2$, $IrTe_2$, $ZrSe_2$, $ZrTe_2$, $TiTe_2$, and $MoTe_2$ exhibit $\Delta\Delta G_H$ within ±0.1 eV. In particular, $ZrSe_2$ has $\Delta\Delta G_H$ of 0.01 eV, the smallest in magnitude, and hence the best HER performance is expected for $ZrSe_2$.

To understand the material dependence of catalytic activity of anion vacancies, we try to identify key physical quantities that affect $\Delta\Delta G_H$. We use the backward elimination method in the multiple linear regression model to find the most correlated quantities among various properties in bulk and vacant systems (see Section 4 in Supporting Information for details of the regression procedure). The final regression result in Figure 4 shows that $\Delta\Delta G_H$ at the vacancy site is highly correlated with

DOI: 10.1021/acs.jpclett.8b00712
J. Phys. Chem. Lett. 2018, 9, 2049–2055

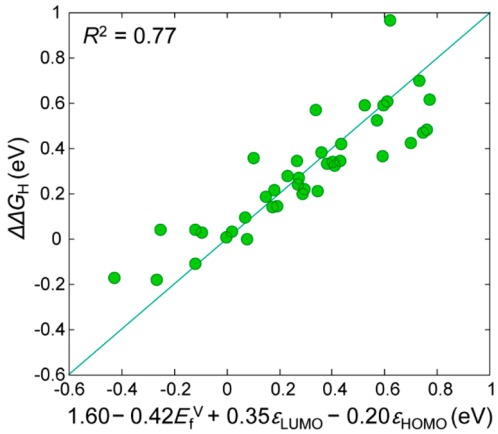

Figure 4. Regression result showing the correlation between hydrogen adsorption free energies on anion vacancy sites and physical parameters such as the vacancy formation energy and LUMO and HOMO levels. The R^2 score of the regression is 0.77.

E_f^V, the lowest unoccupied molecular orbital (LUMO) level, and the highest occupied molecular orbital (HOMO) level of the defective TMDs ($\Delta\Delta G_H \approx 1.60 - 0.42E_f^V + 0.35\varepsilon_{LUMO} - 0.20\varepsilon_{HOMO}$). This can be rationalized as follows: First, in hydrogen adsorption on the vacancy site, localized defect states hybridize with the hydrogen state to form a bonding state that partly compensates the loss of bond energy due to the vacancy formation. Therefore, the more energy is required for vacancy formation, the more hydrogen adsorption is favored. Second, the excess electrons after filling the bonding state occupy the LUMO level of the defective system, as shown in Figure 3d–f. Thus lower LUMO level facilitates the hydrogen adsorption. The strong correlation between LUMO and the hydrogen adsorption energy was also reported for the nondefective TMD catalyst.[48] Note that in group 5 TMDs atomic arrangements around V_X in TMDs in the H phase restore the original positions of nondefective TMDs, removing a_1' and e' states associated with the structural distortion (see Figure 3e). Lastly, the bonding state effectively takes two electrons from HOMO level, so higher HOMO levels tend to strengthen the hydrogen adsorption. For instance, the bonding state in MoS_2 takes two electrons from the a_1 state, and an excess electron occupies the LUMO level (e state). (See Figure 3f.) The foregoing analysis explains why the vacancy site is more active than defect-free basal planes.

In the case of large V_X concentrations, the interaction among defect–defect states as well as defect-host states modulates the hydrogen adsorption property at the vacancy site. As a result, TMDs including $MoTe_2$, $ReSe_2$, $MoSe_2$, MoS_2, $ReTe_2$, WSe_2, and $HfTe_2$ that were outside the optimal window at low ρ_V appear in Figure 2c as promising candidates.

Assuming the linear dependence of $\Delta\Delta G_H$ on ρ_V, which is indeed a good approximation for S vacancy in MoS_2 for $\rho_V >$ 6%,[27] we estimate the HER activity at the intermediate ρ_V. Figure 5 shows TMDs that can potentially exhibit good HER activity at certain values of ρ_V between 6.25 (low) and 25% (high) with $\Delta\Delta G_H$ close to zero. We classify these TMDs into four types: Anion vacancies of MoS_2, WSe_2, $ReSe_2$, and $ReTe_2$ in type I show relatively high $\Delta\Delta G_H$ at low ρ_V, but it decreases to ~0 eV at high ρ_V. Thus they can be a good HER catalyst when the anion vacancy is created in large concentrations. (In ref 27, the external strain was applied in addition to increasing ρ_V.) In type II consisting of $MoSe_2$ and $MoTe_2$, $\Delta\Delta G_H$ of anion

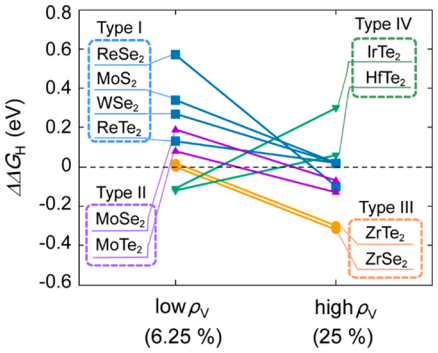

Figure 5. Trend of hydrogen adsorption free energy as a function of the vacancy concentration. See the text for details of each type.

vacancy, which is small and positive at low ρ_V, also reduces with increasing ρ_V but becomes negative at high ρ_V. Considering the stability issue in tellurides,[49] $MoSe_2$ would be more favorable than $MoTe_2$ at intermediate ρ_V. TMDs classified as type III such as $ZrSe_2$ and $ZrTe_2$ show the almost ideal value of $\Delta\Delta G_H$ at low ρ_V, while they gradually become inactive at high ρ_V due to overly strong bonding of hydrogen. Unlike types I–III, $\Delta\Delta G_H$ of anion vacancy in type IV TMDs increases with ρ_V. Because these materials have negative $\Delta\Delta G_H$ at low ρ_V, increasing ρ_V to ~10% would be beneficial, but further creation of vacancy would undermine the HER activity.

In conclusion, we have explored the HER efficiency of anion vacancies of stable phases of various TMDs based on the hydrogen adsorption free energy. Our results show that many inert TMD basal planes become candidates for HER catalysts upon introducing anion vacancies, supporting that the vacancy engineering could be a strong design principle for every TMD. We found that $ZrSe_2$ and $ZrTe_2$ have similar hydrogen-binding energies to that of Pt, the best HER catalyst, when the vacancy density is low. Moreover, fine-tuning is possible by adjusting vacancy concentrations. At proper vacancy densities, MoS_2, $MoSe_2$, $MoTe_2$, $ReSe_2$, $ReTe_2$, WSe_2, $IrTe_2$, and $HfTe_2$ are expected to show the optimal HER activity with the hydrogen-binding energy approaching the thermoneutral condition. The experimental verification of the present theoretical prediction is in demand. By providing insights into the design principles to catalytically activate 2D materials using point defects, we believe that the present study will contribute to identifying alternative catalysts that may eventually replace Pt.

■ ASSOCIATED CONTENT

Supporting Information

The Supporting Information is available free of charge on the ACS Publications website at DOI: 10.1021/acs.jpclett.8b00712.

Determination of chemical potential of X, Dependence of ΔG_H on exchange-correlational functionals, V_X levels and structural distortion in group 5 TMDs, and backward elimination method in multiple linear regression. (PDF)

■ AUTHOR INFORMATION

Corresponding Authors

*Y.K.: E-mail: thehoya84@gmail.com.
*S.H.: E-mail: hansw@snu.ac.kr.

ORCID

Ho Won Jang: 0000-0002-6952-7359
Youngho Kang: 0000-0003-4532-0027

DOI: 10.1021/acs.jpclett.8b00712
J. Phys. Chem. Lett. 2018, 9, 2049–2055

Present Addresses
[‖]K.Y.: Korea Institute of Energy Research, 152 Gajeong-ro, Yuseong-gu, Daejeon 34129, Korea.
[⊥]K.Y.K.: LGE Yangjae R&D campus, 38, Baumoe-ro, Seocho-gu, Seoul 06763, Korea.

Author Contributions
[§]J.L. and S.K. contributed equally.

Notes
The authors declare no competing financial interest.

■ ACKNOWLEDGMENTS

This work was supported by the Samsung Research Funding Center of Samsung Electronics. The computations were performed at the KISTI supercomputing center (grant no. KSC-2017-C3-0019). Y.K. acknowledges the Fundamental Research Program (PNK5260) of the Korea Institute of Materials Science, Republic of Korea.

■ REFERENCES

(1) Mazloomi, K.; Gomes, C. Hydrogen as an Energy Carrier: Prospects and Challenges. *Renewable Sustainable Energy Rev.* **2012**, *16*, 3024−3033.
(2) Turner, J. A. Sustainable Hydrogen Production. *Science* **2004**, *305*, 972−974.
(3) Du, P.; Eisenberg, R. Catalysts Made of Earth-Abundant Elements (Co, Ni, Fe) for Water Splitting: Recent Progress and Future Challenges. *Energy Environ. Sci.* **2012**, *5*, 6012−6021.
(4) Liu, Q.; Tian, J.; Cui, W.; Jiang, P.; Cheng, N.; Asiri, A. M.; Sun, X. Carbon Nanotubes Decorated with CoP Nanocrystals: A Highly Active Non-Noble-Metal Nanohybrid Electrocatalyst for Hydrogen Evolution. *Angew. Chem.* **2014**, *126*, 6828−6832.
(5) Popczun, E. J.; McKone, J. R.; Read, C. G.; Biacchi, A. J.; Wiltrout, A. M.; Lewis, N. S.; Schaak, R. E. Nanostructured Nickel Phosphide as an Electrocatalyst for the Hydrogen Evolution Reaction. *J. Am. Chem. Soc.* **2013**, *135*, 9267−9270.
(6) Merki, D.; Hu, X. Recent Developments of Molybdenum and Tungsten Sulfides as Hydrogen Evolution Catalysts. *Energy Environ. Sci.* **2011**, *4*, 3878−3888.
(7) Vesborg, P. C. K.; Seger, B.; Chorkendorff, I. Recent Development in Hydrogen Evolution Reaction Catalysts and Their Practical Implementation. *J. Phys. Chem. Lett.* **2015**, *6*, 951−957.
(8) Benck, J. D.; Hellstern, T. R.; Kibsgaard, J.; Chakthranont, P.; Jaramillo, T. F. Catalyzing the Hydrogen Evolution Reaction (HER) with Molybdenum Sulfide Nanomaterials. *ACS Catal.* **2014**, *4*, 3957−3971.
(9) Laursen, A. B.; Kegnæs, S.; Dahl, S.; Chorkendorff, I. Molybdenum Sulfides—Efficient and Viable Materials for Electro- and Photoelectrocatalytic Hydrogen Evolution. *Energy Environ. Sci.* **2012**, *5*, 5577−5591.
(10) Cheng, L.; Huang, W.; Gong, Q.; Liu, C.; Liu, Z.; Li, Y.; Dai, H. Ultrathin WS_2 Nanoflakes as a High-Performance Electrocatalyst for the Hydrogen Evolution Reaction. *Angew. Chem., Int. Ed.* **2014**, *53*, 7860−7863.
(11) Voiry, D.; Yamaguchi, H.; Li, J.; Silva, R.; Alves, D. C.; Fujita, T.; Chen, M.; Asefa, T.; Shenoy, V. B.; Eda, G.; Chhowalla, M. Enhanced Catalytic Activity in Strained Chemically Exfoliated WS_2 Nanosheets for Hydrogen Evolution. *Nat. Mater.* **2013**, *12*, 850−855.
(12) Chia, X.; Ambrosi, A.; Lazar, P.; Sofer, Z.; Pumera, M. Electrocatalysis of Layered Group 5 Metallic Transition Metal Dichalcogenides (MX_2, M= V, Nb, and Ta; X= S, Se, and Te). *J. Mater. Chem. A* **2016**, *4*, 14241−14253.
(13) Toh, R. J.; Sofer, Z.; Pumera, M. Catalytic Properties of Group 4 Transition Metal Dichalcogenides (MX_2; M= Ti, Zr, Hf; X= S, Se, Te). *J. Mater. Chem. A* **2016**, *4*, 18322−18334.
(14) Deng, D.; Novoselov, K. S.; Fu, Q.; Zheng, N.; Tian, Z.; Bao, X. Catalysis with Two-Dimensional Materials and Their Heterostructures. *Nat. Nanotechnol.* **2016**, *11*, 218−230.
(15) Wang, Y.; Li, Y.; Chen, Z. Not Your Familiar Two Dimensional Transition Metal Disulfide: Structural and Electronic Properties of the PdS_2 Monolayer. *J. Mater. Chem. C* **2015**, *3*, 9603−9608.
(16) Yin, Y.; Han, J.; Zhang, Y.; Zhang, X.; Xu, P.; Yuan, Q.; Samad, L.; Wang, X.; Wang, Y.; Zhang, Z.; et al. Contributions of Phase, Sulfur Vacancies, and Edges to the Hydrogen Evolution Reaction Catalytic Activity of Porous Molybdenum Disulfide Nanosheets. *J. Am. Chem. Soc.* **2016**, *138*, 7965−7972.
(17) Andoshe, D. M.; Jeon, J. M.; Kim, S. Y.; Jang, H. W. Two-Dimensional Transition Metal Dichalcogenide Nanomaterials for Solar Water Splitting. *Electron. Mater. Lett.* **2015**, *11*, 323−335.
(18) Li, Y.; Wang, H.; Xie, L.; Liang, Y.; Hong, G.; Dai, H. MoS_2 Nanoparticles Grown on Graphene: An Advanced Catalyst for the Hydrogen Evolution Reaction. *J. Am. Chem. Soc.* **2011**, *133*, 7296−7299.
(19) Hinnemann, B.; Moses, P. G.; Bonde, J.; Jørgensen, K. P.; Nielsen, J. H.; Horch, S.; Chorkendorff, I.; Nørskov, J. K. Biomimetic Hydrogen Evolution: MoS_2 Nanoparticles as Catalyst for Hydrogen Evolution. *J. Am. Chem. Soc.* **2005**, *127*, 5308−5309.
(20) Jaramillo, T. F.; Jørgensen, K. P.; Bonde, J.; Nielsen, J. H.; Horch, S.; Chorkendorff, I. Identification of Active Edge Sites for Electrochemical H_2 Evolution from MoS_2 Nanocatalysts. *Science* **2007**, *317*, 100−102.
(21) Zeng, M.; Li, Y. Recent Advances in Heterogeneous Electrocatalysts for the Hydrogen Evolution Reaction. *J. Mater. Chem. A* **2015**, *3*, 14942−14962.
(22) Tsai, C.; Abild-Pedersen, F.; Nørskov, J. K. Tuning the MoS_2 Edge-Site Activity for Hydrogen Evolution via Support Interactions. *Nano Lett.* **2014**, *14*, 1381−1387.
(23) Kong, D.; Wang, H.; Cha, J. J.; Pasta, M.; Koski, K. J.; Yao, J.; Cui, Y. Synthesis of MoS_2 and $MoSe_2$ Films with Vertically Aligned Layers. *Nano Lett.* **2013**, *13*, 1341−1347.
(24) Voiry, D.; Salehi, M.; Silva, R.; Fujita, T.; Chen, M.; Asefa, T.; Shenoy, V. B.; Eda, G.; Chhowalla, M. Conducting MoS_2 Nanosheets as Catalysts for Hydrogen Evolution Reaction. *Nano Lett.* **2013**, *13*, 6222−6227.
(25) Lukowski, M. A.; Daniel, A. S.; Meng, F.; Forticaux, A.; Li, L.; Jin, S. Enhanced Hydrogen Evolution Catalysis from Chemically Exfoliated Metallic MoS_2 Nanosheets. *J. Am. Chem. Soc.* **2013**, *135*, 10274−10277.
(26) Ambrosi, A.; Sofer, Z.; Pumera, M. 2H→ 1T Phase Transition and Hydrogen Evolution Activity of MoS_2, $MoSe_2$, WS_2 and WSe_2 Strongly Depends on the MX_2 Composition. *Chem. Commun.* **2015**, *51*, 8450−8453.
(27) Li, H.; Tsai, C.; Koh, A. L.; Cai, L.; Contryman, A. W.; Fragapane, A. H.; Zhao, J.; Han, H. S.; Manoharan, H. C.; Abild-Pedersen, F.; et al. Activating and Optimizing MoS_2 Basal Planes for Hydrogen Evolution Through the Formation of Strained Sulphur Vacancies. *Nat. Mater.* **2016**, *15*, 48−53.
(28) Lin, L.; Miao, N.; Wen, Y.; Zhang, S.; Ghosez, P.; Sun, Z.; Allwood, D. A. Sulfur-Depleted Monolayered Molybdenum Disulfide Nanocrystals for Superelectrochemical Hydrogen Evolution Reaction. *ACS Nano* **2016**, *10*, 8929−8937.
(29) Escalera-López, D.; Niu, Y.; Yin, J.; Cooke, K.; Rees, N. V.; Palmer, R. E. Enhancement of the Hydrogen Evolution Reaction from Ni-MoS_2 Hybrid Nanoclusters. *ACS Catal.* **2016**, *6*, 6008−6017.
(30) Ouyang, Y.; Ling, C.; Chen, Q.; Wang, Z.; Shi, L.; Wang, J. Activating Inert Basal Planes of MoS_2 for Hydrogen Evolution Reaction Through the Formation of Different Intrinsic Defects. *Chem. Mater.* **2016**, *28*, 4390−4396.
(31) Nørskov, J. K.; Bligaard, T.; Logadottir, A.; Kitchin, J. R.; Chen, J. G.; Pandelov, S.; Stimming, U. Trends in the Exchange Current for Hydrogen Evolution. *J. Electrochem. Soc.* **2005**, *152*, J23−J26.
(32) Tsai, C.; Chan, K.; Nørskov, J. K.; Abild-Pedersen, F. Theoretical Insights into the Hydrogen Evolution Activity of Layered Transition Metal Dichalcogenides. *Surf. Sci.* **2015**, *640*, 133−140.
(33) Greeley, J.; Nørskov, J. K.; Kibler, L. A.; El-Aziz, A. M.; Kolb, D. M. Hydrogen Evolution Over Bimetallic Systems: Understanding the Trends. *ChemPhysChem* **2006**, *7*, 1032−1035.

DOI: 10.1021/acs.jpclett.8b00712
J. Phys. Chem. Lett. 2018, 9, 2049−2055

(34) Greeley, J.; Jaramillo, T. F.; Bonde, J.; Chorkendorff, I.; Nørskov, J. K. Computational High-Throughput Screening of Electrocatalytic Materials for Hydrogen Evolution. *Nat. Mater.* **2006**, *5*, 909−913.
(35) Kresse, G.; Furthmüller, J. Efficient Iterative Schemes for *Ab Initio* Total-Energy Calculations Using a Plane-Wave Basis Set. *Phys. Rev. B: Condens. Matter Mater. Phys.* **1996**, *54*, 11169−11186.
(36) Blöchl, P. E. Projector Augmented-Wave Method. *Phys. Rev. B: Condens. Matter Mater. Phys.* **1994**, *50*, 17953−17979.
(37) Perdew, J. P.; Burke, K.; Ernzerhof, M. Generalized Gradient Approximation Made Simple. *Phys. Rev. Lett.* **1996**, *77*, 3865−3868.
(38) Bengtsson, L. Dipole Correction for Surface Supercell Calculations. *Phys. Rev. B: Condens. Matter Mater. Phys.* **1999**, *59*, 12301−12304.
(39) Belsky, A.; Hellenbrandt, M.; Karen, V. L.; Luksch, P. New Developments in the Inorganic Crystal Structure Database (ICSD): Accessibility in Support of Materials Research and Design. *Acta Crystallogr., Sect. B: Struct. Sci.* **2002**, *58*, 364−369.
(40) Chen, X.; Gu, Y.; Tao, G.; Pei, Y.; Wang, G.; Cui, N. Origin of Hydrogen Evolution Activity on MS_2 (M= Mo or Nb) Monolayers. *J. Mater. Chem. A* **2015**, *3*, 18898−18905.
(41) Hong, X.; Chan, K.; Tsai, C.; Nørskov, J. K. How Doped MoS_2 Breaks Transition-Metal Scaling Relations for CO_2 Electrochemical Reduction. *ACS Catal.* **2016**, *6*, 4428−4437.
(42) Atkins, P. *Physical Chemistry*, 9th ed; Oxford University Press: Oxford, U.K., 2014.
(43) Gileadi, E. *Electrosorption*; Plenum Press: New York, 1967.
(44) Pandey, M.; Vojvodic, A.; Thygesen, K. S.; Jacobsen, K. W. Two-Dimensional Metal Dichalcogenides and Oxides for Hydrogen Evolution: A Computational Screening Approach. *J. Phys. Chem. Lett.* **2015**, *6*, 1577−1585.
(45) Ataca, C.; Şahin, H.; Ciraci, S. Stable, Single-Layer MX_2 Transition-Metal Oxides and Dichalcogenides in a Honeycomb-Like Structure. *J. Phys. Chem. C* **2012**, *116*, 8983−8999.
(46) Gong, C.; Zhang, H.; Wang, W.; Colombo, L.; Wallace, R. M.; Cho, K. Band Alignment of Two-Dimensional Transition Metal Dichalcogenides: Application in Tunnel Field Effect Transistors. *Appl. Phys. Lett.* **2013**, *103*, 053513−053516.
(47) Pandey, M.; Rasmussen, F. A.; Kuhar, K.; Olsen, T.; Jacobsen, K. W.; Thygesen, K. S. Defect-Tolerant Monolayer Transition Metal Dichalcogenides. *Nano Lett.* **2016**, *16*, 2234−2239.
(48) Wang, J.; Liu, J.; Zhang, B.; Ji, X.; Xu, K.; Chen, C.; Miao, L.; Jiang, J. The Mechanism of Hydrogen Adsorption on Transition Metal Dichalcogenides as Hydrogen Evolution Reaction Catalyst. *Phys. Chem. Chem. Phys.* **2017**, *19*, 10125−10132.
(49) Zhou, L.; Xu, K.; Zubair, A.; Liao, A. D.; Fang, W.; Ouyang, F.; Lee, Y. − H.; Ueno, K.; Saito, R.; Palacios, T.; et al. Large-Area Synthesis of High-Quality Uniform Few-Layer $MoTe_2$. *J. Am. Chem. Soc.* **2015**, *137*, 11892−11895.

DOI: 10.1021/acs.jpclett.8b00712
J. Phys. Chem. Lett. 2018, 9, 2049−2055